nature astronomy

Article

https://doi.org/10.1038/s41550-024-02295-8

Complex rotational dynamics of the neutron star in Hercules X-1 revealed by X-ray polarization

Received: 13 July 2023

Accepted: 13 May 2024

Published online: 18 June 2024

Check for updates

A list of authors and their affiliations appears at the end of the paper

In an accreting X-ray pulsar, a neutron star accretes matter from a companion star through an accretion disk. The magnetic field of the rotating neutron star disrupts the inner edge of the disk, funnelling the gas to flow onto the poles on its surface. Hercules X-1 is a prototypical persistent X-ray pulsar about 7 kpc from Earth. Its emission varies on three distinct timescales: the neutron star rotates every 1.2 s, it is eclipsed by its companion each 1.7 d, and the system exhibits a superorbital period of 35 d, which has remained stable since its discovery. Several lines of evidence point to the source of this variation as the precession of the accretion disk or that of the neutron star. Despite the many hints over the past 50 yr, the precession of the neutron star itself has yet not been confirmed or refuted. X-ray polarization measurements (probing the spin geometry of Her X-1) with the Imaging X-ray Polarimetry Explorer suggest that free precession of the neutron star crust sets the 35 d period; this has the important implication that its crust is somewhat asymmetric by a few parts per ten million.

Hercules X-1 was observed by the Imaging X-ray Polarimetry Explorer (IXPE)[1] over 17–24 2022 February (255 ks), at the beginning of the 35 d precession cycle, the so-called main-on state[2] and again in January and February 2023 during the short-on state (148 ks) and the main-on state (245 ks), as shown in Fig. 1. The gas-pixel detector on IXPE registers the arrival time, sky position and energy of each X-ray photon and uses the photoelectric effect to provide an estimate of the position angle of each photon[3]. During each observation, photon arrival events registered between energies of 2 and 8 keV within 52 arcsec of the position of the source were extracted for analysis. We did not subtract the background in the analysis as a bright source such as Hercules X-1 dominates the background over a very large region of the detector[4]. The times of photon arrivals were corrected for the motion of IXPE around the barycentre of the Solar System and for the orbit of the neutron star about its companion; consequently, the times of arrival are calculated for a frame of reference moving with the neutron star. The details of the data reduction are outlined in the methods section of Doroshenko et al.[2].

Our analysis focuses on the geometry of the spinning neutron star over the pulsar rotation period and the superorbital period. We used a maximum likelihood technique[5] to determine the mean polarization properties averaged over the pulsar orbit, as shown in Fig. 1. These results (averaged over the orbit and rotational phase) agree with those reported previously[6]; however, polarization measurements averaged over the rotational phase cannot accurately probe the rotational state of the neutron star. Measurements averaged over the rotational phase follow the polarization of the dominant pulsed component at each superorbital phase; therefore, we also measured the polarization as a function of rotational phase during the different superorbital states of the system, as presented in Fig. 2. We fixed the phase of zero in the two main-on epochs to the peak of the X-ray light curve. For the short-on, we fixed the phase of 1/2 to the peak of the light curve, in agreement with previous work[7]. Our results do not depend on the choice of phasing among the epochs. We tracked the observed polarization angle (PA) as the star rotated to determine the geometry of the spinning neutron star and to study the geometry as the system evolved through the superorbital period. As already apparent in Fig. 1, the source appears much fainter during the short-on than during the main-on (this is often attributed to occultation by the accretion disk[7]), so the count rate for the short-on in Fig. 2 must be inflated by a factor of ten to be visible clearly. The polarization degree (PD) in the two main-on epochs is about 5% to 15%, and in the short-on, it is about two times larger. The pulse profile and PD are consistent between the two

e-mail: heyl@phas.ubc.ca

https://doi.org/10.1038/s41550-024-02295-8

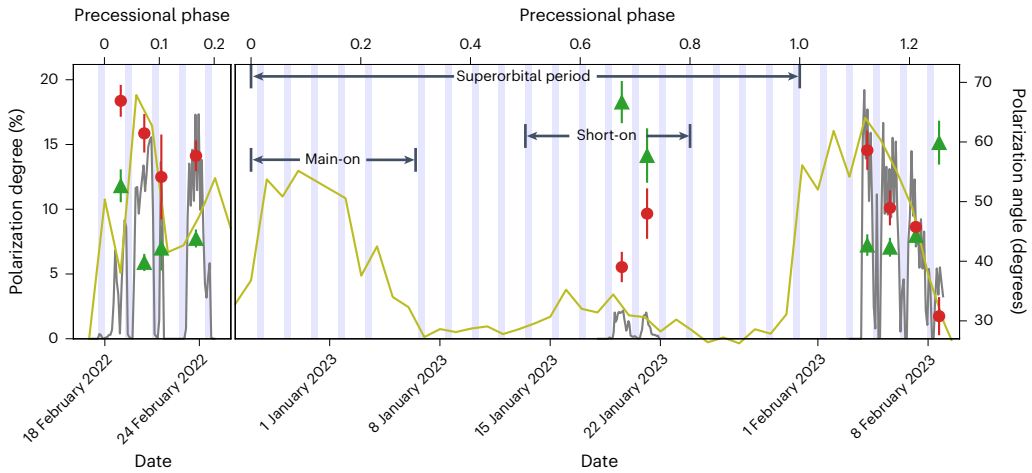

Fig. 1 | Evolution of the observed flux, PA and PD from Her X-1. Flux from IXPE is depicted by a grey curve and from Swift by olive. PD is depicted by green triangles (left *y* axis), and PA by red circles (right *y* axis). Time and phase of the 35 d superorbital precession cycle are given by the two *x* axes. The turn-on time on 18 February 2022 was estimated from IXPE data. Those of 26 December 2022 and 30 January 2023 were estimated from Swift data. The main-on lasts from precessional phase 0 to 0.3 (26 December 2022 to 8 January 2023), and the short-on lasts from 0.5 to 0.8 (15–25 January 2023). These phases repeat every 34.84 d (the superorbital period). The reported values and the uncertainties correspond to the mean values and 1σ (68%) confidence intervals and agree with previously reported results[2,6]. The shaded regions depict the intervals when the companion star and its accretion stream eclipse the neutron star. We define the superorbital phase of zero to coincide with the beginning of the main-on[2,7].

main-on epochs[8]. More dramatic changes are apparent when one examines the PA as a function of spin phase. The evolutions of the PA over the spin period during the two main-on epochs are nearly identical up to an offset. Over the course of the year, between the two main-on epochs, the mean PA decreased by 9.2° ± 1.8°. The variation of the PA during the short-on, on the other hand, was much smaller than during the main-on.

The neutron star in Hercules X-1 does not rotate as an isolated rigid body[9]. The magnetic field, whose geometry we measured through the polarization, is anchored to the rigid crust of the neutron star and transmits torques from the accretion flow. For Hercules X-1, the total precessional torque exerted magnetically by the accretion disk on the neutron star crust is[10,11]

$$N_{\rm tot}^{\rm prec} \approx 2\sin^2\theta\sin 2\beta\left(\frac{B_{\rm p}}{3\times10^{12}\,{\rm G}}\right)^2\left(\frac{R_{\rm m}}{1000\,{\rm km}}\right)^{-3}\times10^{36}\,{\rm dyn\,cm},$$

where $B_{\rm p}$ is the magnetic field strength at the pole of the neutron star[12], $R_{\rm m}$ is radius of the inner edge of the accretion disk and β is the misalignment angle between the angular momentum of the spin of the neutron star and the angular momentum of the orbit. The dependence on the angle between the spin axis and the magnetic axis (θ) depends on the details of the magnetic interaction at the surface of the disk; the result given here is for a hybrid model. For a fully diamagnetic or magnetically threaded disk, $\sin^2\theta$ is replaced by $3\cos^2\theta-1$. Furthermore, the magnetic field exerts an additional torque on the disk that tends to warp it[11]:

$$N_{\rm tot}^{\rm warp} \approx 0.2\cos^2\theta\sin 2\beta\left(\frac{B_{\rm p}}{3\times10^{12}\,{\rm G}}\right)^2\left(\frac{R_{\rm m}}{1000\,{\rm km}}\right)^{-3}\times10^{36}\,{\rm dyn\,cm}.$$

Both of these torques vanish if the accretion disk lies above the rotational equator of the neutron star ($\beta=0$); however, the misalignment between the neutron star spin and the orbit was measured to be at least 24° (ref. 2), so $\sin 2\beta > 0.7$. Thus, both the precessional and warping torques are finite and vary with the angle between the spin axis and the magnetic axis (θ). Furthermore, the magnetic field passes through the core of the neutron star where it interacts with the core superfluid, so the core also exerts torques on the crust. As the moment of inertia of the crust is about one hundredth of the entire neutron star (10^{43} g cm^2)[13], the crust itself reaches an approximate torque equilibrium, so that the net torque on the crust is small[9].

The measured PA probes the instantaneous rotation axis of the neutron star crust. If the neutron star crust is prolate, oblate or triaxial and if the spin axis does not coincide with a symmetry axis of the crust, the rotation axis can move relative to the crust (that is precess in the body frame), even in the absence of a net torque over the precession period of the neutron star. This would change the evolution of the PA with spin phase. We can infer that the neutron star is nearly symmetric to within a few parts per ten million from the ratio of the spin period of 1.2 s to the potential precession period of 35 d (the superorbital period)[14]. If the angular momentum of the crust is conserved, the orientation of the rotation axis relative to the observer (in the space frame) remains constant also to within a few parts per ten million, and therefore, any observed changes in the orientation in the space frame are a hallmark of a net torque on the neutron star crust.

To measure the orientation of the rotation axis relative to the crust of the neutron star and relative to us, we fitted the photon arrival times and photo-electron angles directly to a rotating vector model (RVM; Methods) of the PA[15]. The RVM measures the instantaneous rotation axis of the neutron star crust in the space frame through the parameters $\chi_{\rm p}$ (the position angle of the rotation axis on the sky in degrees east of north) and $i_{\rm p}$ (the inclination of the rotation axis with respect to the line of sight) and in the body frame through the parameters θ (the magnetic obliquity or the angle between the magnetic pole and rotation axis) and ϕ_0 (the longitude of the magnetic pole relative to the point of zero phase). The coloured curves in Fig. 2 depict the best-fitting RVM models for the measured photo-electron trajectories. The best-fitting parameters for these fits are given in Table 1, and the covariances are shown in Extended Data Figs. 1–5. Figure 3 depicts the varying geometry schematically. The values for the first main-on epoch agree with those measured by Doroshenko et al.[2] within the uncertainties. To examine whether the parameters changed over the course of a single main-on phase, we fitted only the data for the first two orbital periods (early epoch 1) and the final orbit (late epoch 1), and we present these results as well. During the first main-on, the RVM parameters did not vary substantially. However, the differences are significant among the three epochs: first main-on, short-on and second main-on. In particular, as indicated by the

https://doi.org/10.1038/s41550-024-02295-8

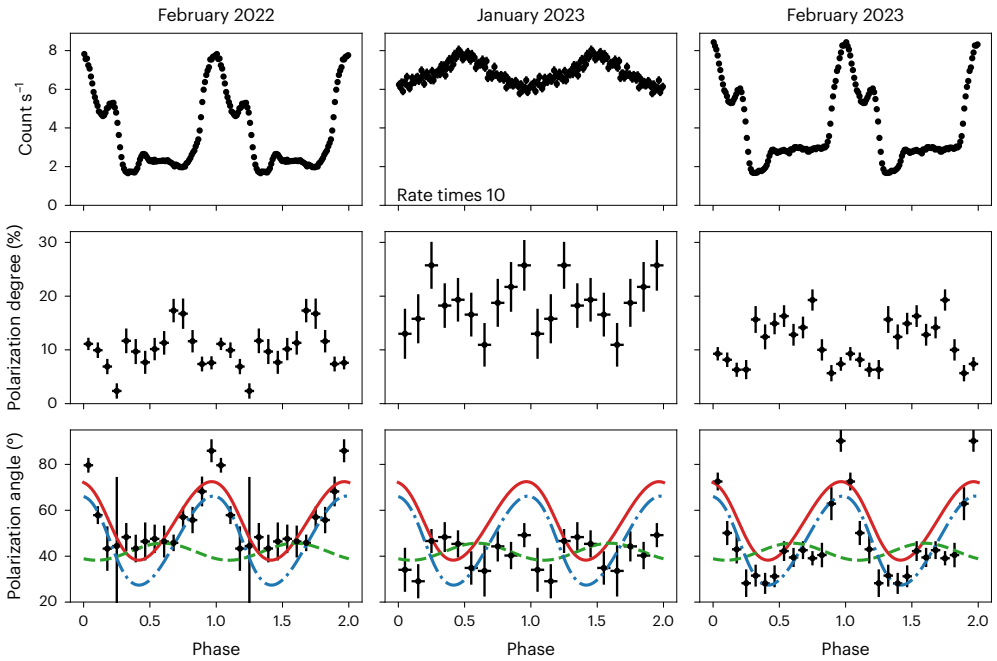

Fig. 2 | IXPE observations of Hercules X-1 as a function of spin phase. The top, middle and bottom rows show with black error bars the IXPE count rate, the PD and the PA, respectively. Left, middle and right columns are for the first main-on (February 2022), the short-on (January 2023) and the second main-on (February 2023), respectively. Error bars indicate $\Delta \log L = 1/2$ and are equivalent to 1σ. The solid red, dashed green and dot-dashed blue curves in the bottom row depict the best-fitting RVM models for the first main-on, the short-on and the second main-on, respectively.

phase-resolved polarimetry, the position angle of the spin axis on the sky (χ_p) changed by 9° ($8.^\circ 6 \pm 2.^\circ 2$) between the two main-on epochs whereas the other parameters remained the same within the uncertainties. This indicates that the angular momentum of the crust changed from February 2022 to February 2023. The average torque to achieve this over the 350 d between the two observations is 3×10^{35} dyn cm, a factor of seven smaller than the torques that the disk applies on the crust.

Furthermore, between the short-on and the latter main-on, there is strong evidence ($p \approx 0.008$) that the angle between the spin axis and the magnetic dipole (θ) is larger during the main-on than during the short-on: $16.0^\circ {}^{+3.1^\circ}_{-4.3^\circ}$ versus $3.7^\circ {}^{+2.6^\circ}_{-1.9^\circ}$. The larger value of θ is reflected in the larger amplitude of modulation in the PA that we noted earlier. In principle, a larger contribution of scattered X-rays could reduce the swing in polarization during the short-on as well, but this would also reduce the PD below what is observed. Furthermore, observations of the winds and corona through the superorbital period[15,16] support the conclusion that scattering did not contribute much to the observed radiation during this epoch. The change in the value of θ between the short-on and the second main-on indicates that the spin axis of the crust moved relative to the magnetic axis of the neutron star. As we do not see evidence of a change of i_p or χ_p over this short 16 d period, we argue that a net torque is not required to account for this precession, so that it is approximately free. Furthermore, the torque that would be required to cause the spin axis to move through a symmetric crust by 12° over 16 d is 6×10^{36} dyn cm. This exceeds the torque that the disk exerts on the crust by a factor of three[10,11] and would very probably also cause the orientation of the spin axis to change with respect to the sky by a comparable amount, which was not observed. Consequently, the approximately free precession of the modestly asymmetric crust over the 35 d superorbital period remains as the most conservative explanation for the observed short-term changes in the geometry. We argue in Methods that the observed PAs are consistent with a prolate[17] or triaxial[18] crust; however, both the angle between the spin axis and the symmetry axis and that between the magnetic pole and the symmetry axis must be smaller than previously proposed[17,18], about 10° rather than 30° or 50°.

The neutron star crust and the core are strongly coupled, and in the absence of torques, the relative motion between them dissipates on a timescale of minutes to hours[9]. The coupling between the crust and the superfluid within the crust is mediated through the pinning and unpinning of vortices on nuclei in the crust in a process called vortex creep. Typically, the lag between the crust and the crust superfluid is larger than that between the crust and the core superfluid. These dissipative processes would dampen the wobbling of the crust over a timescale of a few hundred years in the absence of external torques. On the other hand, the external torques, supplied by accretion in the case of Hercules X-1, can support an equilibrium in which the external torques on the crust balance both the torques between the crust and the core superfluid and the larger torque between the crust and the crust superfluid, so the crust itself can exhibit a precession approximately free of torques. In fact, an external torque, like the one exerted by accretion, can drive the crust to precess. The amplitude of the precession would then depend on the long-term behaviour of the external torque. This torque increases with the sine of the misalignment angle between the spin axis and the figure axis of the neutron star crust, so larger misalignments require larger torques to maintain, and a stable equilibrium with approximately free precession of the crust can be achieved.

As the crust executes its precessional motion, the torque exerted on the disk by the magnetic field of the neutron star will also vary on the same timescale because the angle between the spin axis and the magnetic axis (θ) changes. These torques excite the precession and warping of the disk, which were invoked to explain the evolution of the system through the superorbital phase, and their variation through the changing value of θ over the precession of the neutron star crust sets the superorbital timescale. From the point of view of the neutron star, these torques serve to maintain the approximate free precession of the crust against internal dissipation, which would dampen the precession within hundreds of years[9]. The amplitude of the precession and, therefore, the magnitude of the internal torques necessary to maintain the precession depend on the mean value of the accretion torques over the damping time of several hundred years. In contrast, the external torques depend on the current accretion. If these two differ by about 10%, the resulting

Table 1 | Best-fitting RVM parameters

	Mean PD (%)	χ_p (deg)	θ (deg)	i_p (deg)	$\phi_0/2\pi$	Precessional phase	$\Delta \log L$ (σ)
First main-on	9.5±0.5	55.4±1.6	$14.5^{+3.0}_{-4.0}$	58^{+28}_{-22}	$0.19^{+0.03}_{-0.02}$	0.088	−1.52
Early	8.6±0.6	57.9±2.1	$16.3^{+3.5}_{-4.1}$	64^{+25}_{-22}	$0.19^{+0.03}_{-0.02}$	0.073	+0.07
Late	9.3±0.7	52.2±2.7	$15.9^{+3.6}_{-4.0}$	85^{+35}_{-37}	$0.22^{+0.05}_{-0.05}$	0.162	+0.05
Short-on	17.8±1.4	41.9±2.2	$3.7^{+2.6}_{-1.9}$	90^{+30}_{-30}	$0.85^{+0.18}_{-0.20}$	0.687	−0.19
Second main-on	9.1±0.5	46.8±1.5	$16.0^{+3.1}_{-4.3}$	56^{+24}_{-20}	$0.20^{+0.02}_{-0.02}$	0.159	+0.48

The observations for the first main-on were taken over 17–24 February 2022, and the early portion corresponds to the first 4 d of this segment. The short-on was observed over 18–21 January 2023, and the second main-on from 3–8 February 2023. The second-to-last column gives the median precession phase for the observation. The final column indicates the quality of the fit. When the data are consistent with the model, the log-likelihood ($\log L$) is normally distributed, and the fit quality in the last column is given in terms of the best-fitting log-likelihood compared to the expected value. Positive values indicate better than expected values. For each parameter, the median and the differences to the 16th to 84th percentiles of the posteriors are given.

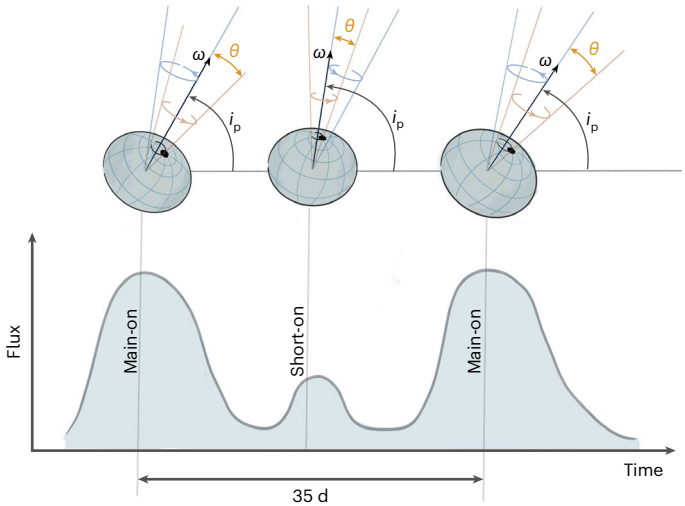

Fig. 3 | Schematic showing the geometry varying through the precession of Hercules X-1. The dark spot on the surface of the neutron star indicates the location of the magnetic pole.

net torque on the crust could result in the observed net precession of the spin axis of the crust on the sky. In fact, continued observations of Hercules X-1 could constrain the mean accretion rate over the past few hundred years as well as details of the crust–superfluid coupling.

Polarization measurements with IXPE have revealed that the PA as a function of spin phase changes over the superorbital period and also over longer timescales. We interpret these observations as signatures of the free precession and forced precession of the crust of the neutron star in Hercules X-1, which confirms that the neutron star itself provides the clock for the superorbital period[19] and reveals that torques also change the angular momentum of the crust on a year-long timescale. This forced precession may account for the anomalous lows in Hercules X-1 and modulations of the superorbital period that occur on a 5 yr timescale[20]. Further polarization observations of Hercules X-1 will probe the interior of the neutron star, in particular the coupling between the crust and the superfluid, as well as the accretion dynamics. Polarization observations of other X-ray binaries with superorbital periods, a common phenomenon in these sources, may verify their underlying clocks.

Methods

Rotating vector model

Although the structure of the magnetic field in the emission region of the pulsar is expected to be complicated[17], the PA of photons from different parts of the emission region are expected to follow the magnetic field direction as they propagate in the highly magnetized plasma surrounding the X-ray pulsar. Even at large distances from the neutron star, where the plasma does not affect the radiation, vacuum birefringence causes the polarized radiation in the magnetosphere to propagate in the ordinary (O) and extraordinary (X) modes, which represent oscillations of the electric field parallel and perpendicular to the plane formed by the local magnetic field and the photon momentum[21,22]. Propagation in the normal modes continues within the so-called polarization limiting radius[23]. For typical X-ray pulsars, this radius is estimated to be about thirty stellar radii[24]. The field is dominated by the dipole component, so the polarization measured at the telescope is expected to be either parallel or perpendicular to the instantaneous projection of the magnetic dipole axis of the star onto the plane of the sky. For this reason, the modulation of the PA with phase is decoupled from the evolution in PD and intensity and should follow the RVM[5,25,26]:

$$\tan(\mathrm{PA}-\chi_\mathrm{p}) = \frac{\sin\theta\sin(\phi-\phi_0)}{\cos i_\mathrm{p}\sin\theta\cos(\phi-\phi_0)-\sin i_\mathrm{p}\cos\theta}, \quad (1)$$

where i_p is the inclination of the angular velocity with respect to the line of sight, χ_p is the position angle of the rotation axis in the plane of the sky, θ is the inclination of the magnetic dipole to the spin axis, ϕ is the spin phase and ϕ_0 is the phase of the rotation when the magnetic dipole axis is closest to the line of sight.

RVM with free precession

To model the polarization direction as a function of rotational and precessional phase, we use the formalism of Euler angles[14] to yield the following expression:

$$\begin{aligned}\tan(\mathrm{PA}-\chi_\mathrm{M}) = {} & [\sin\theta_\mathrm{B}\sin\varphi\cos(\psi-\psi_\mathrm{B})+\sin\theta_\mathrm{B}\sin(\psi-\psi_\mathrm{B})\cos\varphi\cos\alpha- \\ & \sin\alpha\cos\theta_\mathrm{B}\cos\varphi][-\sin i_\mathrm{M}\sin\theta_\mathrm{B}\sin\alpha\sin(\psi-\psi_\mathrm{B})- \\ & -\sin i_\mathrm{M}\cos\theta_\mathrm{B}\cos\alpha-\sin\theta_\mathrm{B}\sin\varphi\sin(\psi-\psi_\mathrm{B})\cos i_\mathrm{M}\cos\alpha+ \\ & \sin\theta_\mathrm{B}\cos i_\mathrm{M}\cos\varphi\cos(\psi-\psi_\mathrm{B})+\sin\varphi\sin\alpha\cos i_\mathrm{M}\cos\theta_\mathrm{B}]^{-1}, \quad (2)\end{aligned}$$

where χ_M is the position angle of the angular momentum on the plane of the sky, θ_B is the angle between the symmetry axis with the largest moment of inertia and the magnetic axis (the magnetic obliquity), φ is the rotation angle, ψ is the precession angle, ψ_B is the longitude of the magnetic axis using the symmetry axis with the smallest moment of inertia as a reference, α is the angle between the angular velocity and the symmetry axis with the largest moment and i_M is the angle between the angular momentum and the line of sight. The angles are depicted in Supplementary Fig. 1.

Because the asymmetry of the moment of inertia is small, the values of χ_M and i_M are nearly constant in the absence of torques;

furthermore, the evolution of the angles in the symmetric case where two of the moments of inertia are equal is straightforward:

$$\psi = 2\pi\nu_{\rm prec}t, \qquad \varphi = 2\pi\nu_{\rm rot}t, \qquad \alpha = \text{constant}. \tag{3}$$

If the star is oblate, the two frequencies have opposite signs, and the precession is retrograde. Even in the biaxial case, the observed rotation frequency (defined as the inverse of the timescale between the crossings of PA through $\chi_{\rm M}$, for example), is not constant through the precession (Supplementary Fig. 2)[18]. The value of $\nu_{\rm rot}$ is the mean rotation frequency over the precession period.

The situation for a triaxial body is somewhat more complicated but also straightforward[14]. Let us define the three eigenvalues of the moment of inertia tensor to be $I_3 > I_2 > I_1$. If we let α_0 be the minimum spin misalignment when the spin axis is nearest to the axis with the smallest moment of inertia (I_1), we can define the following parameters:

$$k^2 = \frac{I_3\,(I_2 - I_1)}{I_1\,(I_3 - I_2)}\tan^2\alpha_0, \qquad n = \frac{I_1(I_3 - I_2)}{I_2(I_3 - I_1)}, \tag{4}$$

where the time parameter through the precession is given by

$$\tau = 4K(k)\nu_{\rm prec}t, \tag{5}$$

where $K(k)$ is a complete elliptic integral of the first kind (ellipk in scipy). The precession rate is

$$\nu_{\rm prec} = \frac{\Omega_{3,0}}{4K(k)}\sqrt{\frac{(I_3 - I_2)(I_3 - I_1)}{I_1 I_2}}, \tag{6}$$

where $\Omega_{3,0}$ is the angular velocity about the minor axis at the time of minimum spin misalignment.

Using the Jacobi elliptic functions (ellipj in scipy), we have

$$\tan\psi(\tau) = \sqrt{n}\,\frac{\mathrm{cn}(\tau|k^2)}{\mathrm{sn}(\tau|k^2)}, \quad \cos\alpha(\tau) = \mathrm{dn}(\tau|k^2)\cos\alpha_0, \tag{7}$$

where $\tan\psi$ is inverted to account for the sign of the numerator and denominator, so the range is zero to 2π (for example by using arctan2). The Jacobi elliptic functions are periodic with a period of $K(k)$, so the functions $\psi(\tau)$ and $\alpha(\tau)$ are also periodic. The expression for the angle ψ ensures that ψ decreases in time, so the precession again is retrograde as expected. The final parameter is the rotational angle φ, which is given by[14]

$$\varphi = \left[2\pi\nu_{\rm rot}t - \frac{2\pi\nu_{\rm rot}}{\Omega_{3,0}}\frac{I_2 - I_1}{\sqrt{(I_3 - I_2)(I_3 - I_1)}}\sqrt{\frac{I_2}{I_1}}\int_0^\tau \cos^2\psi\,\mathrm{d}\tau'\right]\left(1 - \frac{I_2 - I_1}{I_1}\langle\cos^2\psi\rangle\right)^{-1}. \tag{8}$$

In an approximation where we neglect the differences in the moments of inertia beyond first order, we have $\Omega_{3,0} \approx 2\pi\nu_{\rm rot}\cos\alpha_0$ and

$$\varphi = 2\pi\nu_{\rm rot}t - \frac{1}{\cos\alpha_0}\frac{I_2 - I_1}{\sqrt{(I_3 - I_2)(I_3 - I_1)}}\int_0^\tau \left(\cos^2\psi - \langle\cos^2\psi\rangle\right)\mathrm{d}\tau'. \tag{9}$$

These two integrals can be expressed in closed form using Jacobi theta functions with complex arguments[14]; however, it is straightforward to integrate them numerically. Although the second term in this expression is explicitly periodic in τ with a period of $K(k)$, the first term is not, so the star does not necessarily return to the same configuration.

Models for the free precession of Hercules X-1

Several models have been proposed for the free precession of the neutron star in Hercules X-1 to explain the superorbital period. Postnov et al.[17] proposed a prolate model to account for the variation in pulse profiles, and Kolesnikov, Shakura and Postnov[18] used a triaxial model to explain the variation in the spin frequency of the star[18]. We first focus on these specific models. The key observables are the minimum and maximum angles between the instantaneous spin axis and the magnetic pole (θ), which determine broadly how the polarization will evolve through the precessional cycle. In all cases, we assumed that the angular momentum of the star makes an angle $i_{\rm M} = 110°$ with respect to the line of sight, as this is the approximate inclination of the orbit[2,27]. We varied this angle from 60° to 120° and verified that changes in this angle made only minor changes to the predicted PAs.

In the prolate model, the ratio of the spin period to the superorbital period is simply the relative difference between the moments of inertia, and the two additional parameters are the time during the precession when the spin axis passes closest to the magnetic axis and the angle between the spin and the symmetry axis of the star (the spin misalignment angle). Two prolate models are depicted in the upper two panels of Supplementary Fig. 3. The upper left one has a spin misalignment of $\alpha = 50°$ and an angle of $\theta_{\rm B} = 30°$ between the symmetry axis and the magnetic pole (magnetic obliquity), as proposed by Postnov et al.[17]. These angles, along with the precession and rotation angles (ψ and φ), are depicted in Supplementary Fig. 1. This model, in blue in the figure, predicts a variation in the PA throughout the precession that is larger than observed (superimposed coloured regions). To achieve better agreement with the observed PAs, the spin misalignment and magnetic obliquity must be reduced to 11° and 8°, respectively (upper right panel). These angles depend modestly on the assumed value of $i_{\rm M}$. Both are smaller if $i_{\rm M} < 50°$ or $i_{\rm M} > 130°$.

Although the triaxial models cannot be solved using elementary functions, the evolution can be expressed in closed form[14,18,28]. In particular, the precession period is determined by the relative difference between the largest and smallest eigenvalues of the moment of inertia[18], taken to be 6.7×10^{-7}. The relative difference between the second largest and smallest eigenvalues is taken[18] to be 2.7×10^{-7}. We examined two pairings for the minimum spin misalignment angle and the magnetic obliquity, 50° and 30°, as postulated by Kolesnikov, Shakura and Postnov[18] (bottom left panel) and 9.5° and 7.5° (bottom right panel of Supplementary Fig. 3). In both cases, the magnetic axis lies towards the intermediate axis of the neutron star. In the bottom left panel, we see that the variation of the PA is larger throughout the entire precession period than observed during either the short-on or the main-on. As with the prolate model, better agreement is achieved by reducing the misalignment angle and the magnetic obliquity. Doing so results in the models in the bottom right panel, which can account for the observed evolution of the polarization over the superorbital period. Furthermore, the frequency variations reported by Kolesnikov, Shakura and Postnov[18] are consistent with free-precession models, and the models that we present here are also consistent with those variations, as depicted in Supplementary Fig. 2.

Data availability

The data used for this analysis are available through High-Energy Astrophysics Science Archive Research Center under IXPE Observation IDs 01001899, 02003801 and 02004001.

Code availability

The software used for this analysis is available at https://github.com/UBC-Astrophysics/IXPE-Analysis.

References

1. Weisskopf, M. C. et al. The Imaging X-ray Polarimetry Explorer (IXPE): pre-launch. *J. Astron. Telesc. Instrum. Syst.* **8**, 026002 (2022).
2. Doroshenko, V. et al. Determination of X-ray pulsar geometry with IXPE polarimetry. *Nat. Astron.* **6**, 1433–1443 (2022).

3. Soffitta, P. et al. The instrument of the Imaging X-ray Polarimetry Explorer. *Astron. J.* **162**, 208 (2021).
4. di Marco, A. et al. Handling background in IXPE polarimetric data. *Astron. J.* **165**, 143 (2023).
5. González-Caniulef, D., Caiazzo, I. & Heyl, J. Unbinned likelihood analysis for X-ray polarization. *Mon. Not. R. Astron. Soc.* **519**, 5902–5912 (2023).
6. Garg, A., Rawat, D., Bhargava, Y., Méndez, M. & Bhattacharyya, S. Flux-resolved spectropolarimetric evolution of the X-ray pulsar Hercules X-1 using IXPE. *Astrophys. J. Lett.* **948**, l10 (2023).
7. Scott, D. M., Leahy, D. A. & Wilson, R. B. The 35 day evolution of the Hercules X-1 pulse profile: evidence for a resolved inner disk occultation of the neutron star. *Astrophys. J.* **539**, 392–412 (2000).
8. Soong, Y., Gruber, D. E., Peterson, L. E. & Rothschild, R. E. Spectral behavior of Hercules X-1: its long-term variability and pulse phase spectroscopy. *Astrophys. J.* **348**, 641 (1990).
9. Alpar, A. & Oegelman, H. Neutron star precession and the dynamics of the superfluid interior. *Astron. Astrophys.* **185**, 196–202 (1987).
10. Lipunov, V. M. & Shakura, N. I. Interaction of the accretion disk with the magnetic field of a neutron star. *Sov. Astron. Lett.* **6**, 14–17 (1980).
11. Lai, D. Magnetically driven warping, precession, and resonances in accretion disks. *Astrophys. J.* **524**, 1030–1047 (1999).
12. Staubert, R. et al. Long-term change in the cyclotron line energy in Hercules X-1. *Astron. Astrophys.* **572**, a119 (2014).
13. Steiner, A. W., Gandolfi, S., Fattoyev, F. J. & Newton, W. G. Using neutron star observations to determine crust thicknesses, moments of inertia, and tidal deformabilities. *Phys. Rev. C* **91**, 015804 (2015).
14. Landau, L. D. & Lifshitz, E. M. *Mechanics* 4th edn, Vol. 1 (Butterworth-Heinemann, 1976).
15. Shakura, N. I. et al. Observations of Her X-1 in low states during SRG/eROSITA all-sky survey. *Astron. Astrophys.* **648**, a39 (2021).
16. Kosec, P. et al. Vertical wind structure in an X-ray binary revealed by a precessing accretion disk. *Nat. Astron.* **7**, 715–723 (2023).
17. Postnov, K. et al. Variable neutron star free precession in Hercules X-1 from evolution of RXTE X-ray pulse profiles with phase of the 35-d cycle. *Mon. Not. R. Astron. Soc.* **435**, 1147–1164 (2013).
18. Kolesnikov, D., Shakura, N. & Postnov, K. Evidence for neutron star triaxial free precession in Her X-1 from Fermi/GBM pulse period measurements. *Mon. Not. R. Astron. Soc.* **513**, 3359–3367 (2022).
19. Suleimanov, V., Potekhin, A. Y. & Werner, K. Models of magnetized neutron star atmospheres: thin atmospheres and partially ionized hydrogen atmospheres with vacuum polarization. *Astron. Astrophys.* **500**, 891–899 (2009).
20. Staubert, R. et al. Two ~35 day clocks in Hercules X-1: evidence for neutron star free precession. *Astron. Astrophys.* **494**, 1025–1030 (2009).
21. Gnedin, Y. N., Pavlov, G. G. & Shibanov, Y. A. The effect of vacuum birefringence in a magnetic field on the polarization and beaming of X-ray pulsars. *Sov. Astron. Lett.* **4**, 117–119 (1978).
22. Pavlov, G. G. & Shibanov, Y. A. Influence of vacuum polarization by a magnetic field on the propagation of electromagnetic waves in a plasma. *Sov. J. Exp. Theor. Phys.* **49**, 741 (1979).
23. Heyl, J. S. & Shaviv, N. J. Polarization evolution in strong magnetic fields. *Mon. Not. R. Astron. Soc.* **311**, 555–564 (2000).
24. Heyl, J. & Caiazzo, I. Strongly magnetized sources: QED and X-ray polarization. *Galaxies* **6**, 76 (2018).
25. Radhakrishnan, V. & Cooke, D. J. Magnetic poles and the polarization structure of pulsar radiation. *Astrophys. Lett.* **3**, 225 (1969).
26. Poutanen, J. Relativistic rotating vector model for X-ray millisecond pulsars. *Astron. Astrophys.* **641**, a166 (2020).
27. Leahy, D. A. & Abdallah, M. H. Hz Her: stellar radius from X-ray eclipse observations, evolutionary state, and a new distance. *Astrophys. J.* **793**, 79 (2014).
28. Shakura, N. I., Postnov, K. A. & Prokhorov, M. E. On some features of free precession of a triaxial body: the case of Her X-1. *Astron. Astrophys.* **331**, l37–l40 (1998).

Acknowledgements

IXPE is a joint US and Italian mission. The US contribution is supported by the National Aeronautics and Space Administration (NASA) and led and managed by its Marshall Space Flight Center, with industry partner Ball Aerospace (Contract NNM15AA18C). The Italian contribution is supported by the Italian Space Agency (Contract ASI-ASI-OHBI-2022-13-I.0 and Agreements ASI-INAF-2022-19-HH.0 and ASI-INFN-2017.13-H0) and its Space Science Data Center (Agreements ASI-INAF-2022-14-HH.0 and ASI-INFN 2021-43-HH.0), and by the Italian National Institute for Astrophysics and the Italian National Institute for Nuclear Physics. This research used data products provided by the IXPE Team (Marshall Space Flight Center, Space Science Data Center, Italian National Institute for Astrophysics and Italian National Institute for Nuclear Physics) and distributed with additional software tools by the High-Energy Astrophysics Science Archive Research Center at NASA's Goddard Space Flight Center. J.H. acknowledges support from the Natural Sciences and Engineering Research Council of Canada through a discovery grant, the Canadian Space Agency through the co-investigator grant program, and computational resources and services provided by Compute Canada, Advanced Research Computing at the University of British Columbia, and the SciServer science platform (www.sciserver.org). D.G.-C. acknowledges support from a fellowship grant from the French National Centre for Space Studies. J.P. and S.S.T. were supported by the Academy of Finland (Grant Nos. 333112 and 349144) and the Väisälä Foundation. V.D. and V.F.S. thank the German Academic Exchange Service (Travel Grant No. 57525212). We used Astropy (http://www.astropy.org), a community-developed core Python package and an ecosystem of tools and resources for astronomy.

Author contributions

J.H. analysed the data and wrote the draft of the paper. J.P. led the work of the IXPE Topical Working Group on Accreting Neutron Stars and contributed to the interpretation and the text. V.D., D.G.-C., I.C., A. Mushtukov., S.S.T., D.M. and V.F.S. contributed to the interpretation of the results and writing of the text. A. Mushtukov created Fig. 3. M.B. and G.G.P. acted as internal referees of the paper and contributed to its interpretation. Other members of the IXPE collaboration contributed to the design of the mission and its science case and the planning of the observations. All authors provided input and comments on the paper.

Competing interests

The authors declare that they have no competing financial interests.

Additional information

Extended data is available for this paper at https://doi.org/10.1038/s41550-024-02295-8.

Supplementary information The online version contains supplementary material available at https://doi.org/10.1038/s41550-024-02295-8.

Correspondence and requests for materials should be addressed to Jeremy Heyl.

Peer review information *Nature Astronomy* thanks the anonymous reviewers for their contribution to the peer review of this work.

Jeremy Heyl[1] ✉, Victor Doroshenko[2], Denis González-Caniulef[3], Ilaria Caiazzo[4], Juri Poutanen[5], Alexander Mushtukov[6], Sergey S. Tsygankov[5], Demet Kirmizibayrak[1], Matteo Bachetti[7], George G. Pavlov[8], Sofia V. Forsblom[5], Christian Malacaria[9], Valery F. Suleimanov[2], Iván Agudo[10], Lucio Angelo Antonelli[11,12], Luca Baldini[13,14], Wayne H. Baumgartner[15], Ronaldo Bellazzini[13], Stefano Bianchi[16], Stephen D. Bongiorno[15], Raffaella Bonino[17,18], Alessandro Brez[13], Niccolò Bucciantini[19,20,21], Fiamma Capitanio[22], Simone Castellano[13], Elisabetta Cavazzuti[23], Chien-Ting Chen[24], Stefano Ciprini[12,25], Enrico Costa[22], Alessandra De Rosa[22], Ettore Del Monte[22], Laura Di Gesu[23], Niccolò Di Lalla[26], Alessandro Di Marco[22], Immacolata Donnarumma[23], Michal Dovčiak[27], Steven R. Ehlert[15], Teruaki Enoto[28], Yuri Evangelista[22], Sergio Fabiani[22], Riccardo Ferrazzoli[22], Javier A. Garcia[4], Shuichi Gunji[29], Kiyoshi Hayashida[30], Wataru Iwakiri[31], Svetlana G. Jorstad[32,33], Philip Kaaret[15], Vladimir Karas[27], Fabian Kislat[34], Takao Kitaguchi[28], Jeffery J. Kolodziejczak[15], Henric Krawczynski[35], Fabio La Monaca[22], Luca Latronico[17], Ioannis Liodakis[36], Simone Maldera[17], Alberto Manfreda[37], Frédéric Marin[38], Andrea Marinucci[23], Alan P. Marscher[32], Herman L. Marshall[39], Francesco Massaro[17,18], Giorgio Matt[16], Ikuyuki Mitsuishi[40], Tsunefumi Mizuno[41], Fabio Muleri[22], Michela Negro[42,43,44], C.-Y. Ng[45], Stephen L. O'Dell[15], Nicola Omodei[26], Chiara Oppedisano[17], Alessandro Papitto[11], Abel Lawrence Peirson[26], Matteo Perri[11,12], Melissa Pesce-Rollins[13], Pierre-Olivier Petrucci[46], Maura Pilia[7], Andrea Possenti[7], Simonetta Puccetti[12], Brian D. Ramsey[15], John Rankin[22], Ajay Ratheesh[22], Oliver J. Roberts[24], Roger W. Romani[26], Carmelo Sgrò[13], Patrick Slane[47], Paolo Soffitta[22], Gloria Spandre[13], Douglas A. Swartz[24], Toru Tamagawa[28], Fabrizio Tavecchio[48], Roberto Taverna[49], Yuzuru Tawara[40], Allyn F. Tennant[15], Nicholas E. Thomas[15], Francesco Tombesi[25,50,51], Alessio Trois[7], Roberto Turolla[49,52], Jacco Vink[53], Martin C. Weisskopf[15], Kinwah Wu[52], Fei Xie[22,54] & Silvia Zane[52]

[1]University of British Columbia, Vancouver, British Columbia, Canada. [2]Institut für Astronomie und Astrophysik, Universität Tübingen, Tübingen, Germany. [3]Institut de Recherche en Astrophysique et Planétologie, UPS-OMP, CNRS, CNES, Toulouse, France. [4]Division of Physics, Mathematics and Astronomy, California Institute of Technology, Pasadena, CA, USA. [5]Department of Physics and Astronomy, University of Turku, Turku, Finland. [6]Department of Physics, University of Oxford, Oxford, UK. [7]INAF Osservatorio Astronomico di Cagliari, Selargius, Italy. [8]Department of Astronomy and Astrophysics, Pennsylvania State University, University Park, PA, USA. [9]International Space Science Institute, Bern, Switzerland. [10]Instituto de Astrofísica de Andalucía-CSIC, Glorieta de la Astronomía s/n, Granada, Spain. [11]INAF Osservatorio Astronomico di Roma, Rome, Italy. [12]Space Science Data Center, Agenzia Spaziale Italiana, Rome, Italy. [13]Istituto Nazionale di Fisica Nucleare, Sezione di Pisa, Pisa, Italy. [14]Dipartimento di Fisica, Università di Pisa, Pisa, Italy. [15]NASA Marshall Space Flight Center, Huntsville, AL, USA. [16]Dipartimento di Matematica e Fisica, Università degli Studi Roma Tre, Rome, Italy. [17]Istituto Nazionale di Fisica Nucleare, Sezione di Torino, Turin, Italy. [18]Dipartimento di Fisica, Università degli Studi di Torino, Turin, Italy. [19]INAF Osservatorio Astrofisico di Arcetri, Florence, Italy. [20]Dipartimento di Fisica e Astronomia, Università degli Studi di Firenze, Florence, Italy. [21]Istituto Nazionale di Fisica Nucleare, Sezione di Firenze, Florence, Italy. [22]INAF Istituto di Astrofisica e Planetologia Spaziali, Rome, Italy. [23]ASI - Agenzia Spaziale Italiana, Rome, Italy. [24]Science and Technology Institute, Universities Space Research Association, Huntsville, AL, USA. [25]Istituto Nazionale di Fisica Nucleare, Sezione di Roma 'Tor Vergata', Rome, Italy. [26]Department of Physics and Kavli Institute for Particle Astrophysics and Cosmology, Stanford University, Stanford, CA, USA. [27]Astronomical Institute of the Czech Academy of Sciences, Prague, Czech Republic. [28]RIKEN Cluster for Pioneering Research, Wako, Japan. [29]Yamagata University, Yamagata-shi, Japan. [30]Osaka University, Suita, Japan. [31]International Center for Hadron Astrophysics, Chiba University, Chiba, Japan. [32]Institute for Astrophysical Research, Boston University, Boston, MA, USA. [33]Department of Astrophysics, St Petersburg State University, St Petersburg, Russia. [34]Department of Physics and Astronomy and Space Science Center, University of New Hampshire, Durham, NH, USA. [35]Physics Department and McDonnell Center for the Space Sciences, Washington University in St Louis, St Louis, MO, USA. [36]Finnish Centre for Astronomy with ESO, University of Turku, Turku, Finland. [37]Istituto Nazionale di Fisica Nucleare, Sezione di Napoli, Naples, Italy. [38]Université de Strasbourg, CNRS, Observatoire Astronomique de Strasbourg, Strasbourg, France. [39]MIT Kavli Institute for Astrophysics and Space Research, Massachusetts Institute of Technology, Cambridge, MA, USA. [40]Graduate School of Science, Division of Particle and Astrophysical Science, Nagoya University, Furo-cho, Chikusa-ku, Nagoya, Japan. [41]Hiroshima Astrophysical Science Center, Hiroshima University, Higashi-Hiroshima, Japan. [42]University of Maryland, Baltimore, MD, USA. [43]NASA Goddard Space Flight Center, Greenbelt, MD, USA. [44]Center for Research and Exploration in Space Science and Technology, NASA/GSFC, Greenbelt, MD, USA. [45]Department of Physics, The University of Hong Kong, Hong Kong, China. [46]Université Grenoble Alpes, CNRS, IPAG, Grenoble, France. [47]Harvard-Smithsonian Center for Astrophysics, Cambridge, MA, USA. [48]INAF Osservatorio Astronomico di Brera, Merate, Italy. [49]Dipartimento di Fisica e Astronomia, Università degli Studi di Padova, Padua, Italy. [50]Dipartimento di Fisica, Università degli Studi di Roma 'Tor Vergata', Rome, Italy. [51]Department of Astronomy, University of Maryland, College Park, MD, USA. [52]Mullard Space Science Laboratory, University College London, Dorking, UK. [53]Anton Pannekoek Institute for Astronomy & GRAPPA, University of Amsterdam, Amsterdam, The Netherlands. [54]Guangxi Key Laboratory for Relativistic Astrophysics, School of Physical Science and Technology, Guangxi University, Nanning, China. ✉e-mail: heyl@phas.ubc.ca

https://doi.org/10.1038/s41550-024-02295-8

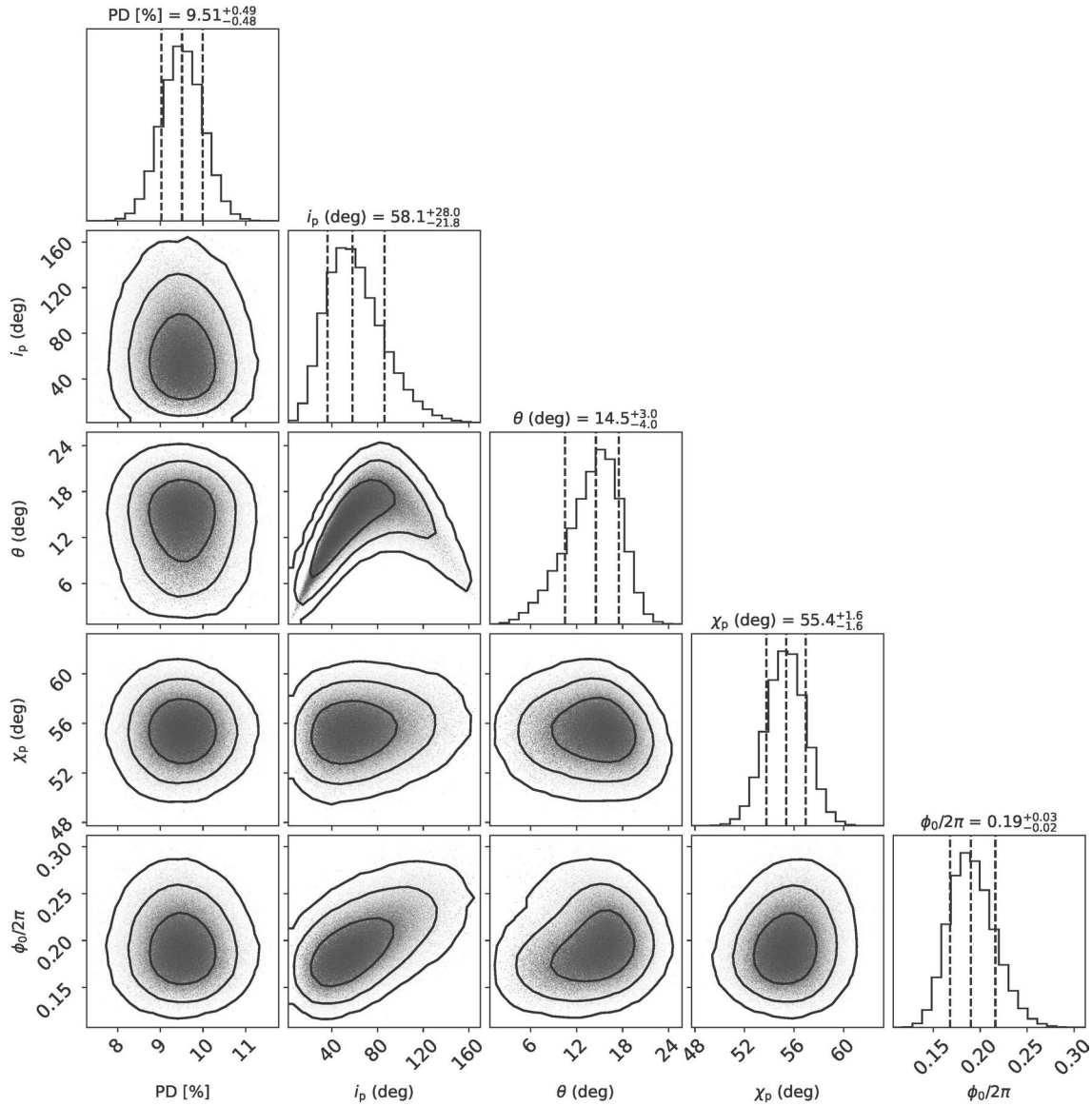

Extended Data Fig. 1 | Posteriors for the RVM for the First Main-On (2022 January). The two-dimensional contours correspond to 68%, 95% and 99% confidence levels. The histograms show the normalized one-dimensional distributions for a given parameter derived from the posterior samples. For each parameter the median and the differences to the 16th to 84th percentiles of the posteriors are given.

https://doi.org/10.1038/s41550-024-02295-8

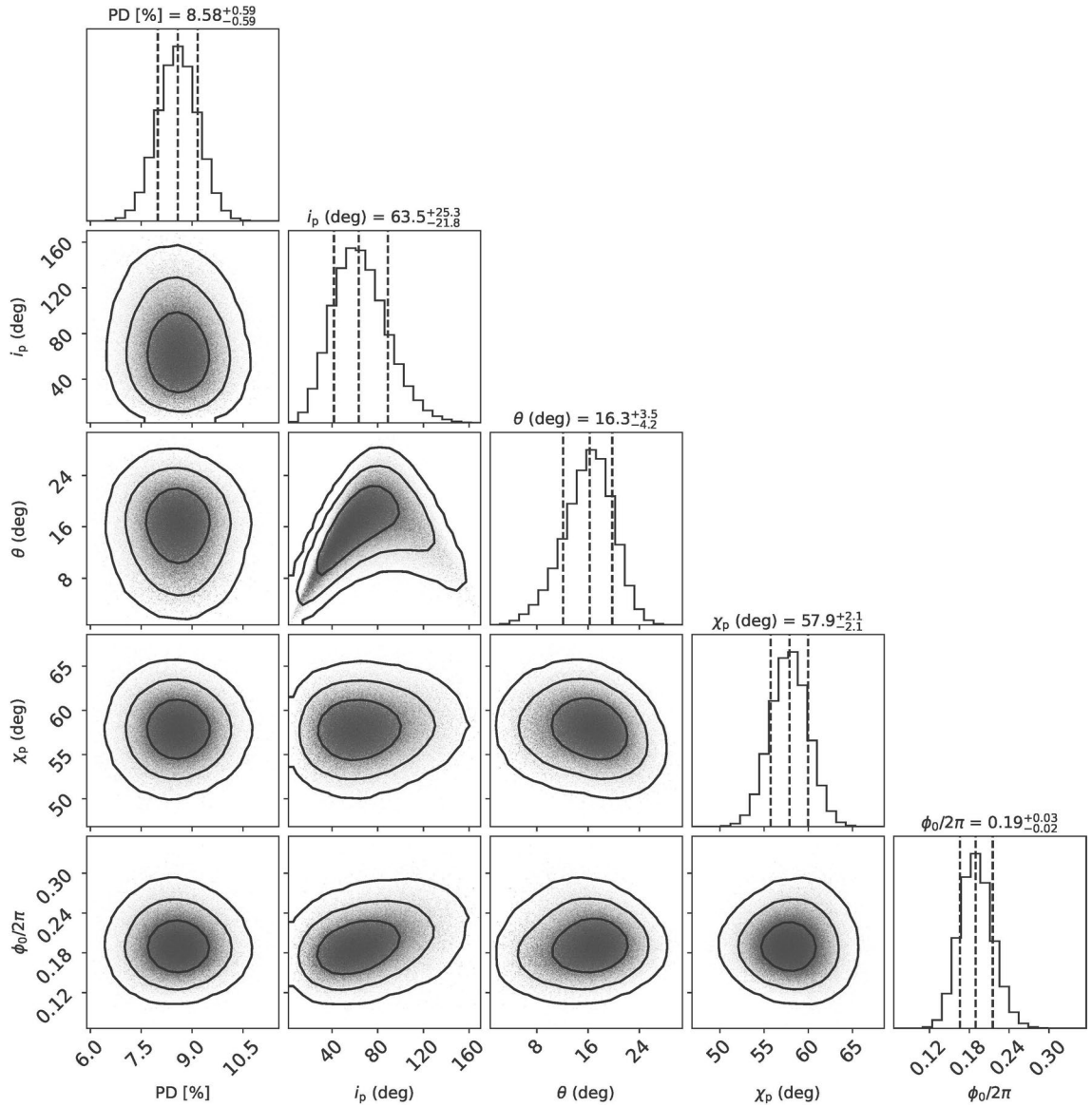

Extended Data Fig. 2 | Posteriors for the RVM for the First Main-On (early). The observations from 2022 February 17 through 21 are analysed as the early portion of the first Main-On. The two- dimensional contours correspond to 68%, 95% and 99% confidence levels. The histograms show the normalized one-dimensional distributions for a given parameter derived from the posterior samples. For each parameter the median and the differences to the 16th to 84th percentiles of the posteriors are given.

https://doi.org/10.1038/s41550-024-02295-8

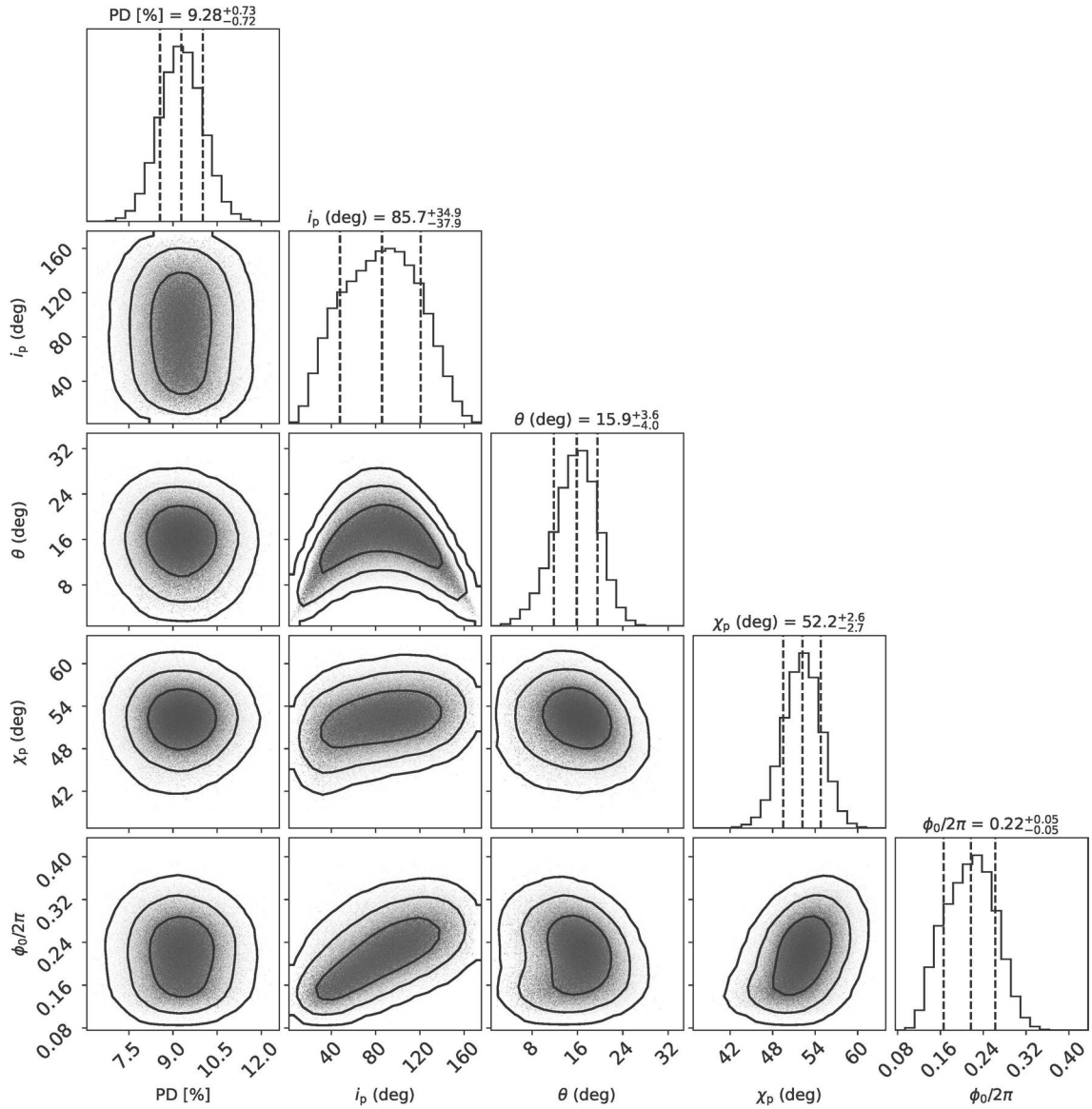

Extended Data Fig. 3 | Posteriors for the RVM for the First Main-On (late). The observations from 2022 February 22 through 24 are analysed as the late portion of the First Main-On. The two- dimensional contours correspond to 68%, 95% and 99% confidence levels. The histograms show the normalized one- dimensional distributions for a given parameter derived from the posterior samples. For each parameter the median and the differences to the 16th to 84th percentiles of the posteriors are given.

https://doi.org/10.1038/s41550-024-02295-8

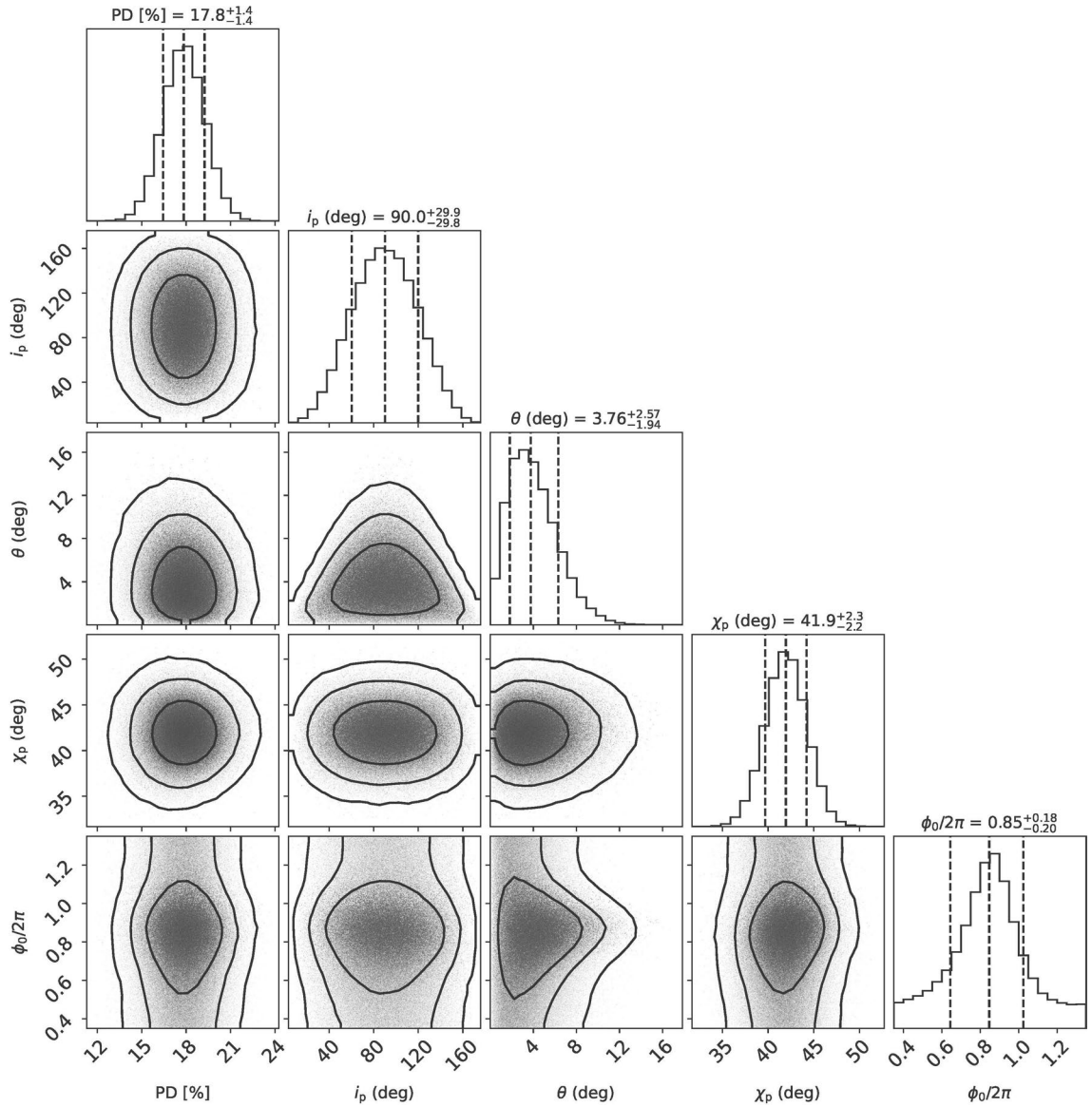

Extended Data Fig. 4 | Posteriors for the RVM for the Short-On (2023 January). The two-dimensional contours correspond to 68%, 95% and 99% confidence levels. The histograms show the normalized one-dimensional distributions for a given parameter derived from the posterior samples. For each parameter the median and the differences to the 16th to 84th percentiles of the posteriors are given.

https://doi.org/10.1038/s41550-024-02295-8

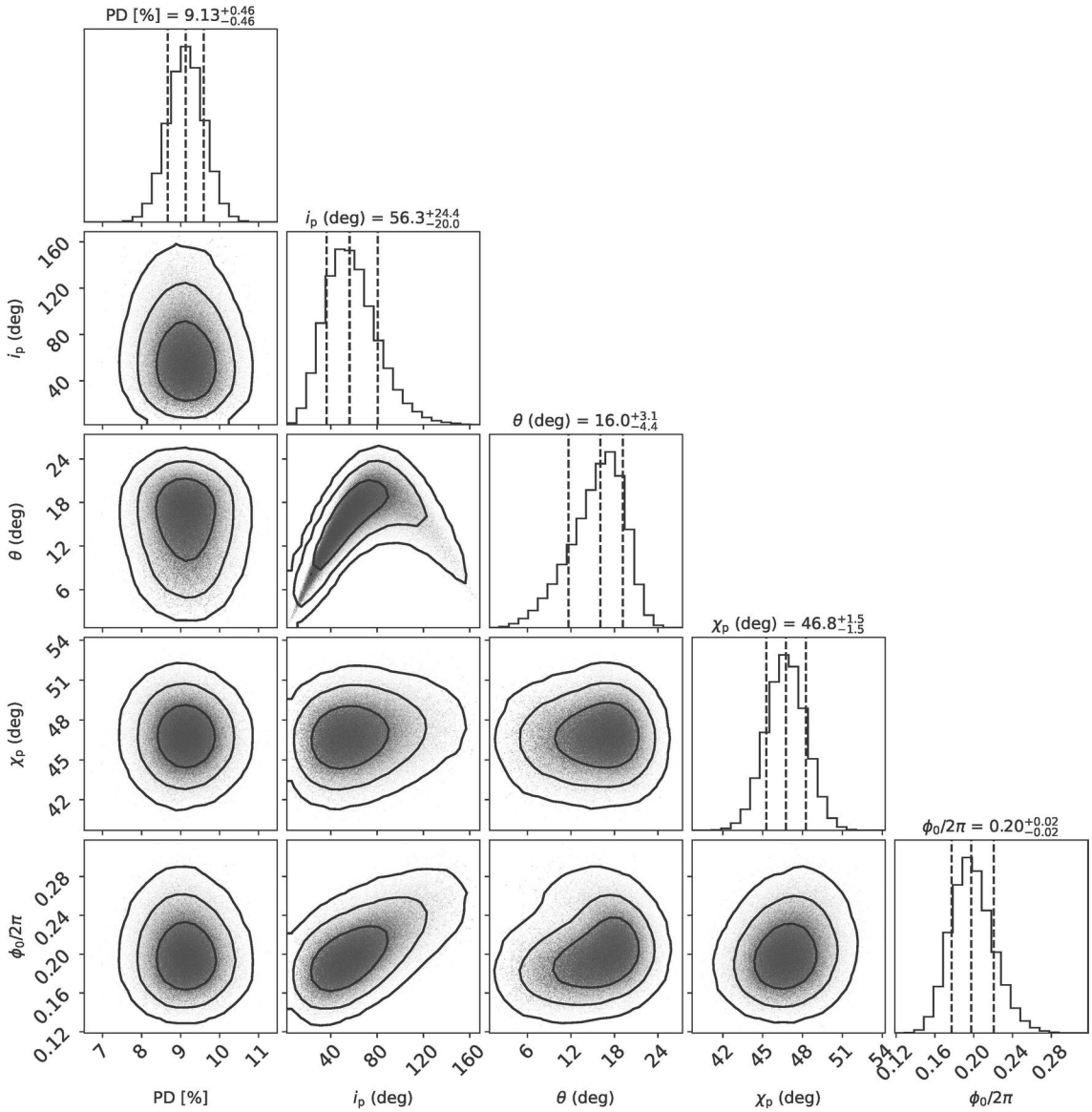

Extended Data Fig. 5 | Posteriors for the RVM for the Second Main- On (2023 February). The two-dimensional contours correspond to 68%, 95% and 99% confidence levels. The histograms show the normalized one-dimensional distributions for a given parameter derived from the posterior samples. For each parameter the median and the differences to the 16th to 84th percentiles of the posteriors are given.